Research Square

Preprints are preliminary reports that have not undergone peer review.
They should not be considered conclusive, used to inform clinical practice,
or referenced by the media as validated information.

Synthesis of Iron-Based ZSM-5 Zeolite via Interzeolite Conversion and Its Application in Phenol Hydroxylation

Yumeng Sun
Lanzhou University of Technology
Mengqi Ding
Lanzhou University of Technology
Xuyang Li
Lanzhou University of Technology
Jinglei Guo
Lanzhou University of Technology
Xinhong Zhao
licpzhaoxh@lut.edu.cn
Lanzhou University of Technology

Research Article

Keywords: Interzeolite conversion, ZSM-5 zeolite, Iron-based catalyst, Phenol hydroxylation

Posted Date: November 16th, 2026

DOI: https://doi.org/10.21203/rs.3.rs-11305090/v1

License: This work is licensed under a Creative Commons Attribution 4.0 International License.
Read Full License

Additional Declarations: No competing interests reported.

Synthesis of Iron-Based ZSM-5 Zeolite via Interzeolite Conversion and Its Application in Phenol Hydroxylation

Yumeng Sun, Mengqi Ding, Xuyang Li, Jinglei Guo, Xinhong Zhao*

School of Petrochemical Technology, Lanzhou University of Technology, Lanzhou, 730050, China

Abstract

Phenol hydroxylation with H_2O_2 over titanium silicalite zeolites is an industrially important route to hydroquinone and catechol. Iron-based catalysts have emerged as promising alternatives owing to their low toxicity, natural abundance, and high efficiency in H_2O_2 activation. Herein, a series of Fe-containing ZSM-5 zeolites (Fe_x-ZSM-5) was synthesized via an ionothermal interzeolite conversion strategy using Beta zeolite as the precursor, and the effects of iron incorporation method and loading on iron speciation and catalytic performance were systematically investigated. Characterization results reveal that iron in the Fe_x-ZSM-5 series predominantly exists as highly dispersed isolated framework Fe^{3+} species and extra-framework oligomeric Fe_xO_y clusters. At comparable iron loading, $Fe_{0.1}$-ZSM-5, which exhibits superior iron dispersion, achieves a phenol conversion of 53.51%, markedly surpassing that of Fe/ZSM-5 (25.83%) prepared by incipient wetness impregnation. Notably, regenerated $Fe_{0.3}$-ZSM-5 displays significantly enhanced dihydroxybenzene selectivity (89.35%) relative to its fresh counterpart (71.29%), owing to the removal of acid-labile iron species. However, the influence of aciditic properties of iron-containing catalysts on the dihydroxybenzene selectivity remains controversial.

Highlights

- A new ionothermal route can convert Beta zeolite into Fe-ZSM-5, offering a faster and greener method for preparing iron-based catalysts.
- Iron introduced during synthesis disperses far better than iron introduced by impregnation, thus achieving a much higher phenol conversion.
- Acidity and iron speciation together determine selectivity: washing away weakly bound iron species during the reaction reduces acid sites, and after regeneration the

* Corresponding author Tel: +86-13919409327
E-mail address: licpzhaoxh@lut.edu.cn *(XH. Zhao)*

dihydroxybenzene selectivity is greatly enhanced.

Keywords: Interzeolite conversion; ZSM-5 zeolite; Iron-based catalyst; Phenol hydroxylation

INTRODUCTION

The phenol hydroxylation reaction is a crucial industrial process for the production of hydroquinone (HQ) and catechol (CAT). These two compounds are extensively used as photographic developers, antioxidants, polymerization inhibitors, and as intermediates in the manufacture of pharmaceuticals and pesticides [1]. Hydrogen peroxide (H_2O_2) is the oxidant with the greatest potential for this reaction, owing to its exceptional atom economy and environmental friendliness [2]. The industrial Enichem process successfully addresses separation challenges through heterogeneous catalysis using titanium silicalite molecular sieves [3, 4]. However, the high cost of titanium precursors continues to motivate the search for efficient, low-cost, and environmentally friendly heterogeneous catalysts.

Iron-based catalysts show great potential for use in phenol hydroxylation because of their low toxicity, low cost, and high efficiency in breaking down H_2O_2 to produce hydroxyl radicals (·OH) [5, 6] It is well established that the catalytic performance of iron-based catalysts is directly impacted by the forms and coordination environment of iron species [7]. Adding iron to zeolites, different iron species can form, such as isolated framework iron ions, iron-oxo clusters inside channels, and surface iron oxide nanoparticles. This can create new catalytic active sites and improve catalytic performance [8]. ZSM-5 zeolite (MFI topology) is an ideal support for iron-based catalysts because of its distinctive channel structure and superior hydrothermal stability [9]. Its pore system, which consists of sinusoidal channels (0.55 nm × 0.51 nm) and straight channels (0.56 nm × 0.53 nm), offers a structural foundation for improving product selectivity and reactant diffusion [10]. Iron-containing ZSM-5 zeolite has been demonstrated to be a superior catalyst for phenol hydroxylation reaction [11].

Conventional zeolite synthesis typically employs amorphous silica and alumina as raw materials in the presence of alkali metal cations and organic structure-directing

agents (OSDAs) via hydrothermal treatment, often requiring protracted crystallization times (2-15 days) [12]. In contrast, the interzeolite conversion method utilizes crystalline zeolites as starting materials to directly transform them into another zeolite with a different topology [13]. This method offers advantages such as fast crystallization rates and high selectivity for specific structures, establishing it as an important approach for zeolite preparation [12]. According to studies, BEA-type zeolite (Beta) and MFI-type zeolite (ZSM-5) share certain secondary building unit 'mor' [14], that help the MFI structure nucleate locally and overcome kinetic barriers in the transition from the BEA structure to the higher framework density MFI structure, allowing for successful conversion [15, 16]. Furthermore, ionic liquids (ILs), owing to their low volatility, high stability, and structure-directing capability, are increasingly used as substitutes for traditional solvents and templates in zeolite synthesis, offering a greener synthetic route [17, 18]. Combining this with the solid-state grinding-assisted synthesis strategy allows for the efficient synthesis of zeolite structures and the incorporation of higher loadings of metal species under mild conditions [19].

In this study, commercial ZSM-5 seeds and Beta zeolite were employed as the starting materials for the synthesis of Fe-ZSM-5 catalysts via an ionothermal interzeolite conversion route, using 1-ethyl-3-methylimidazolium bromide as the ionic liquid, tetrapropylammonium bromide as the OSDA, ammonium fluoride as the mineralizer, and $FeCl_2$ as the iron source. To investigate the influence of iron incorporation method and loading, a reference catalyst (denoted as Fe/ZSM-5) with a comparable iron loading was prepared by incipient wetness impregnation using commercial ZSM-5 support with a similar silica-to-alumina ratio. The effects of iron incorporation amount and incorporation method on the structure, physicochemical properties, and iron species states of the materials were methodically examined using characterization techniques such as XRD, SEM, EDS, N_2 physisorption, FT-IR, Raman, NH_3-TPD, UV-Vis diffuse reflectance spectra, and H_2-TPR. Phenol hydroxylation was used as a probe reaction to assess the catalytic performance.

MATERIALS AND METHODS

Materials

The reagents used in this study include: Beta zeolite (SiO_2/Al_2O_3 = 5, Tianjin Nanhua Catalyst Co., Ltd.), Beta zeolite (SiO_2/Al_2O_3 = 25, Tianjin Nanhua Catalyst Co., Ltd.), ZSM-5 zeolite (SiO_2/Al_2O_3 = 46, Tianjin Nanhua Catalyst Co., Ltd.), ZSM-5 zeolite (SiO_2/Al_2O_3 = 85, Tianjin Nanhua Catalyst Co., Ltd.), tetrapropylammonium bromide (denoted as TPABr, 98%, Shanghai Aladdin Biochemical Technology Co., Ltd.), 1-ethyl-3-methylimidazolium bromide (denoted as ILs, 98%, Shanghai Macklin Biochemical Technology Co., Ltd.), NH_4F (98%, Shanghai Myrell Chemical Technology Co., Ltd.), $FeCl_2$ (99.7%, Tianjin BASF Chemical Co., Ltd.), phenol (99.5%, Shanghai Aladdin Biochemical Technology Co., Ltd.), H_2O_2 (30%, Tianjin Baishi Chemical Industry Co., Ltd.), and deionized water. All commercially available reagents were used without further purification.

Table 1 Synthesis Conditions for Fe_x-ZSM-5 (x = 0, 0.1, 0.2, 0.3) Zeolites

Sample	Beta: NH_4F: TPABr: Seed: ILs: H_2O: $FeCl_2$ (mass ratio)	Time (h)	Temperature (℃)	Crystalline phase
0-NH_4F	0.8: 0: 0.304: 0.02: 5.0: 0.304	96	180	Beta
0.5-NH_4F	0.8: 0.5: 0.304: 0.02: 5.0: 0.304	96	180	ZSM-5
Fe_0-ZSM-5	0.8: 1.0: 0.304: 0.02: 5.0: 0.304	96	180	ZSM-5
0-TPABr	0.8: 1.0: 0: 0.02: 5.0: 0.304	96	180	Beta
0.152-TPABr	0.8: 1.0: 0.152: 0.02: 5.0: 0.304	96	180	ZSM-5
0-seed	0.8: 1.0: 0.304: 0: 5.0: 0.304	96	180	ZSM-5
0.04-seed	0.8: 1.0: 0.304: 0.04: 5.0: 0.304	96	180	ZSM-5
160-T	0.8: 1.0: 0.304: 0.02: 5.0: 0.304	96	160	ZSM-5
200-T	0.8: 1.0: 0.304: 0.02: 5.0: 0.304	96	200	ZSM-5
24-t	0.8: 1.0: 0.304: 0.02: 5.0: 0.304	24	180	ZSM-5
48-t	0.8: 1.0: 0.304: 0.02: 5.0: 0.304	48	180	ZSM-5
72-t	0.8: 1.0: 0.304: 0.02: 5.0: 0.304	72	180	ZSM-5
120-t	0.8: 1.0: 0.304: 0.02: 5.0: 0.304	120	180	ZSM-5
25-SA [a]	0.8: 1.0: 0.304: 0.02: 5.0: 0.304	96	180	ZSM-5

$Fe_{0.1}$-ZSM-5	0.8: 1.0: 0.304: 0.02: 5.0: 0.304: 0.1	96	180	Fe-ZSM-5
$Fe_{0.2}$-ZSM-5	0.8: 1.0: 0.304: 0.02: 5.0: 0.304: 0.2	96	180	Fe-ZSM-5
$Fe_{0.3}$-ZSM-5	0.8: 1.0: 0.304: 0.02: 5.0: 0.304: 0.3	96	180	Fe-ZSM-5

[a] Synthesized with Beta zeolite of SiO_2/Al_2O_3 = 25. All other samples were prepared using Beta zeolite of SiO_2/Al_2O_3 = 5 as the starting material.

Catalyst preparation

Beta zeolite was used as the starting material in an ionothermal system to create Fe-ZSM-5 zeolite utilizing the interzeolite conversion process [14, 20]. The particular synthesis process was as follows: In a mortar, Beta zeolite (SiO_2/Al_2O_3 =5, unless specified otherwise), TPABr, ZSM-5 seeds (SiO_2/Al_2O_3 = 46), NH_4F, 1-ethyl-3-methylimidazolium bromide, $FeCl_2$, and H_2O were combined in a mass ratio of 0.800 Beta: (0-1.000) NH_4F: (0-0.304) TPABr: (0-0.040) Seed: 5.000 ILs: 0.304 H_2O: (0-0.300) $FeCl_2$, ground for 20 minutes. The mixture was subsequently transferred to a 10 mL Teflon-lined stainless-steel autoclave and maintained at predetermined temperatures for set durations to allow for crystallization. The specific synthesis conditions are provided in Table 1. The autoclave was cooled to room temperature following crystallization. Centrifugation was used to repeatedly wash the solid product with ethanol and deionized water until the supernatant was clear. The as-synthesized zeolite powder was then obtained by drying it for 12 hours at 80 ℃ in a drying oven. The as-synthesized powder was calcined in a muffle furnace under an air atmosphere by heating to 550 ℃ at a ramp rate of 2 ℃/min and holding for 4 h to obtain the Fe-ZSM-5 zeolite catalyst.

Commercial ZSM-5 zeolite (SiO_2/Al_2O_3 = 85) was pelletized to determine its water absorption capacity, and iron was then loaded via the incipient wetness impregnation method. An appropriate amount of $FeCl_2$ corresponding to a nominal iron loading of 3 wt% was dissolved in the volume of deionized water calculated based on the water absorption. The zeolite was impregnated with this solution. After impregnation for 24 h, the sample was dried at 80 ℃ for 12 h. The resultant solid was calcined in an air-filled muffle furnace by heating it to 550 ℃ at a ramp rate of 2 ℃ per

minute and holding it there for 4 hours. The obtained sample was denoted as Fe/ZSM-5.

Catalyst characterization

A Rigaku D/Max-2400 diffractometer (Japan) was used to measure X-ray diffraction (XRD) patterns. Using the formula (1) shown below, relative crystallinity was computed from the XRD data. A FESEM 5000 field emission scanning electron microscope (In situ Instrument Technology Co., Ltd., China) was used for scanning electron microscopy (SEM) and energy-dispersive X-ray spectroscopy (EDS) mapping. A Micromeritics ASAP 2460 automatic gas adsorption analyzer (USA) was used to determine N_2 physisorption isotherms. A Micromeritics AutoChem II 2920 automatic programmed temperature chemical adsorption analyzer (USA) was used to perform temperature-programmed desorption of ammonia (NH_3-TPD). A Thermo Scientific Nicolet iS5 spectrometer (China) fitted with an iD1 transmission attachment was used to record Fourier transform infrared (FT-IR) spectra. A Tianmei RM5C confocal Raman microscope (Shanghai, China) was used to gather Raman spectra. An Agilent Cary 5000 UV-Vis-NIR spectrophotometer (China) was used to record ultraviolet-visible (UV-Vis) diffuse reflectance spectra. A Micromeritics AutoChem II 2920 automatic programmed temperature chemical adsorption analyzer (USA) was used to perform temperature-programmed reduction of hydrogen (H_2-TPR).

$$\text{Relative crystallinity}=\frac{\Sigma \text{ integration area of XRD peaks of sample}}{\Sigma \text{ integration area of XRD peaks of reference sample}}\times 100\% \quad (1)$$

Evaluation of Catalytic Performance in Phenol Hydroxylation

The phenol hydroxylation reaction was carried out in a three-necked flask equipped with a reflux condenser and wrapped in aluminum foil to protect the reaction mixture from light. To guarantee a steady and consistent reaction temperature, the flask was submerged in an oil bath with magnetic stirring. The precise process was as follows: the three-necked flask was filled with 2 g of phenol, 24 mL of deionized water, and 0.1 g of catalyst in that order. The reaction was started by adding 2.25 mL of H_2O_2 aqueous solution using a micropipette after the mixture had been heated to 50 ℃.

An LC2030 high-performance liquid chromatograph (Techcomp, Shanghai, China)

fitted with a reversed-phase C18 column (5 μm, 4.6 × 250 mm) was used to evaluate the reaction products. A 2: 3 v/v methanol/water combination flowed at a rate of 1.0 mL/min as the mobile phase. The UV detector's detecting wavelength was 277 nm, and the injection volume was 20 μL. Samples (0.2 mL) were withdrawn at regular intervals during the reaction. After dilution, the concentrations of phenol and product were analyzed using the external standard method. The following formulas were used to determine phenol conversion (X_{PH}), product selectivity (S), and total dihydroxybenzene yield (Y_{DHB}):

$$X_{PH}=\frac{n_0(PH)-n(PH)}{n_0(PH)}\times 100\% \quad (2)$$

$$S_{CAT}=\frac{n(CAT)}{n_0(PH)-n(PH)}\times 100\% \quad (3)$$

$$S_{HQ}=\frac{n(HQ)}{n_0(PH)-n(PH)}\times 100\% \quad (4)$$

$$S_{DHB}=S_{CAT}+S_{HQ} \quad (5)$$

$$Y_{DHB}=X_{PH}\times S_{DHB} \quad (6)$$

Here, the initial and final molar concentrations of phenol are represented by n_0(PH) and n(PH), respectively; the final molar concentrations of catechol and hydroquinone are represented by n(CAT) and n(HQ), respectively; and the selectivity for catechol, hydroquinone, and their total selectivity is represented by S_{CAT}, S_{HQ}, and S_{DHB}.

RESULTS AND DISCUSSION

Catalyst Characterization

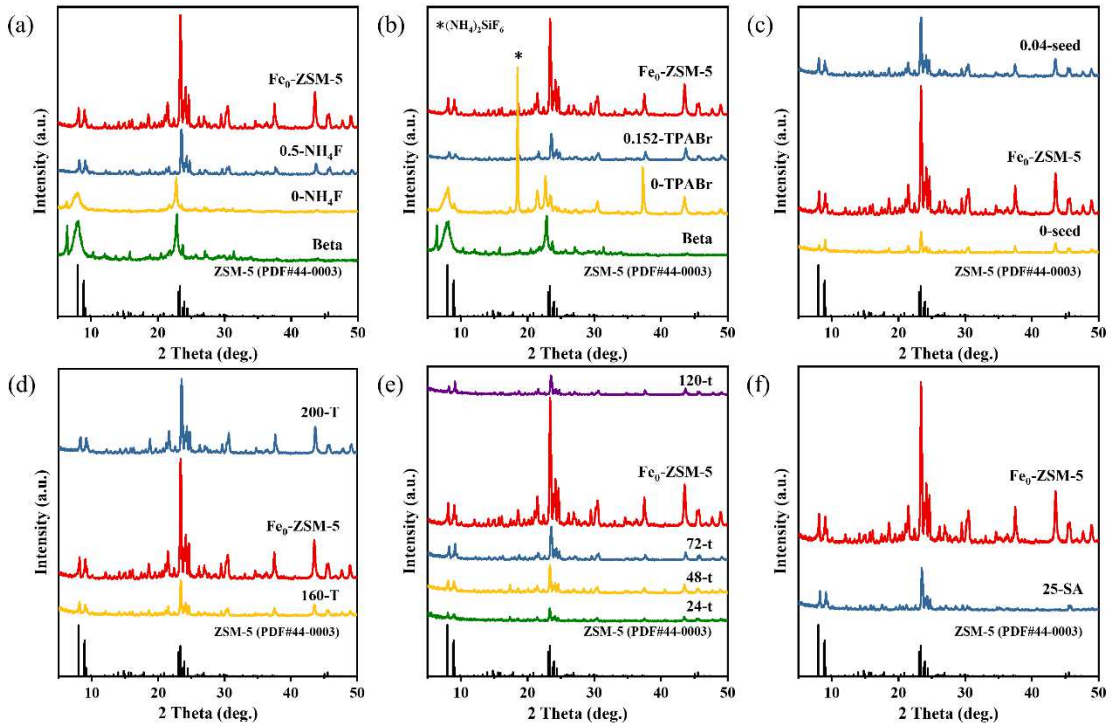


Figure 1 XRD patterns of samples synthesized with varying (a) NH_4F amount, (b) OSDA amount, (c) seed amount, (d) crystallization temperature, (e) crystallization time, and (f) starting zeolite Si/Al ratio

Synthesis conditions were first systematically optimized by varying the amounts of NH_4F/ OSDA/ seeds, crystallization temperature, crystallization time, and the SiO_2/Al_2O_3 ratio of the starting Beta zeolite. The XRD results for the obtained products are shown in Figure 1. With the exception of the 0-NH_4F and 0-TPABr samples, all other samples showed distinctive MFI structure diffraction peaks, suggesting that NH_4F or the OSDA was essential in guiding the conversion of Beta zeolite into ZSM-5. Comprehensive evaluation of all XRD results revealed that the ZSM-5 sample with the highest crystallinity was obtained under the following conditions: Beta (SiO_2/Al_2O_3 = 5): NH_4F: TPABr: Seed: ILs: H_2O = 0.80: 1.0: 0.304: 0.020: 5.0: 0.304, 180 ℃, 96 h. Based on this optimization, iron sources were introduced into this optimal synthesis system in subsequent experiments to prepare a series of Fe-ZSM-5 samples with varying iron contents.

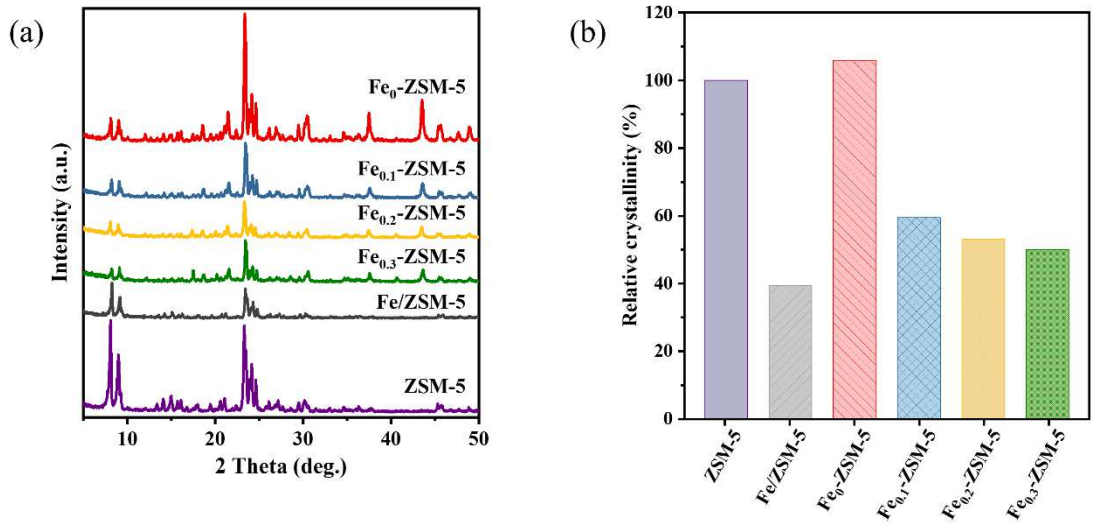


Figure 2 XRD patterns (a) and relative crystallinity (b) of Fe-ZSM-5 samples synthesized via interzeolite conversion and Fe/ZSM-5 prepared by impregnation

XRD results of the samples with different iron incorporation amounts and incorporation methods are shown in Figure 2(a). All iron-containing samples exhibited characteristic diffraction peaks of the MFI structure, indicating the successful synthesis of Fe-ZSM-5 zeolites. Nevertheless, the diffraction peak intensities of the Fe_x-ZSM-5 (x = 0.1, 0.2, 0.3) samples were significantly lower than those of the Fe_0-ZSM-5 sample, indicating that increasing iron incorporation hinders crystal formation and decreases zeolite crystallinity [21]. Similarly, Fe/ZSM-5 had a lower crystallinity than commercial ZSM-5 (Figure 2(b)). Furthermore, no obvious diffraction peaks attributable to iron oxides were observed in the XRD patterns, indicating that the iron species were highly dispersed or present below the detection limit [22].

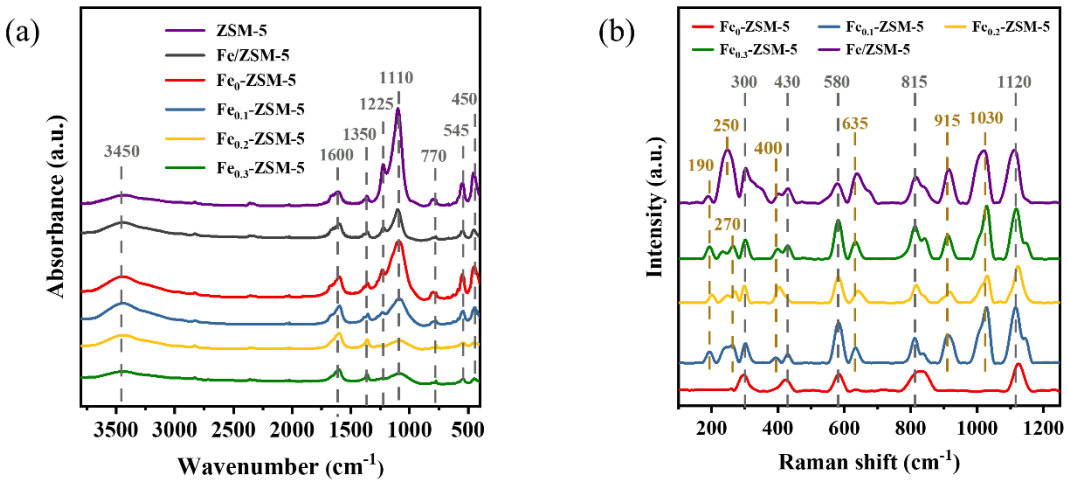


Figure 3 (a) FT-IR spectra and (b) Raman spectra of Fe/ZSM-5 prepared by impregnation and Fe-ZSM-5 synthesized via interzeolite conversion

The structure of Fe-ZSM-5 and Fe/ZSM-5 samples was firstly characterized using infrared spectroscopy. In the FT-IR spectra (Figure 3(a)), the region 2500-3800 cm^{-1} corresponds to hydroxyl vibrations, while the region 400-1300 cm^{-1} corresponds to framework vibrations [23]. The asymmetric stretching vibration of Si-O-Si in the double five-membered rings (d5r) of the pentasil building unit is responsible for the absorption band at 545 cm^{-1}, which is typical of the MFI structure [24]. Absorption bands at 450, 770, 1110, and 1225 cm^{-1} are attributed to zeolite phase-specific Si-O-T bending, symmetric Si-O-T stretching, and asymmetric Si-O-Si stretching between SiO_4 tetrahedra [25]. The band at 1600 cm^{-1} is attributed to the H-O-H bending vibration of adsorbed water, while the bands at 1350 cm^{-1} and 3450 cm^{-1} are assigned to the bending and stretching vibrations of Si-(OH)-Al, respectively, with the latter being characteristic of Brønsted acid sites associated with tetrahedrally coordinated aluminum in the zeolite framework [26, 27].

Additionally, structural characterization was done using Raman spectroscopy with an excitation wavelength of 532 nm; the findings are displayed in Figure 3(b). The MFI structure's distinctive spectral characteristics are peaks at 300, 430, 580, and 815 cm^{-1} [28]. The breathing vibrations of the zeolite's six-membered, five-membered, and double rings are responsible for the maxima at 300, 430, and 580 cm^{-1}, respectively [29]. The symmetric stretching vibration of Si-O-Si in the ZSM-5 framework is responsible for the peak at 815 cm^{-1} [30].

As a result of the addition of iron species, the four iron-containing samples similarly showed clear peaks at 190, 250, 400, 635, and 915 cm^{-1}. The Fe-O-Si symmetric stretching vibration of a small fraction of isolated tetrahedral iron is responsible for the peak at 915 cm^{-1}, whereas iron oxides are responsible for the remaining peaks [31]. The asymmetric stretching vibration of Si-O-Si next to framework iron atoms is mostly responsible for the peak that appears at 1030 cm^{-1}. The iron-free sample also showed the peak at 1120 cm^{-1}, which may be related to local structural distortions brought on by the zeolite's low crystallinity [29, 32].

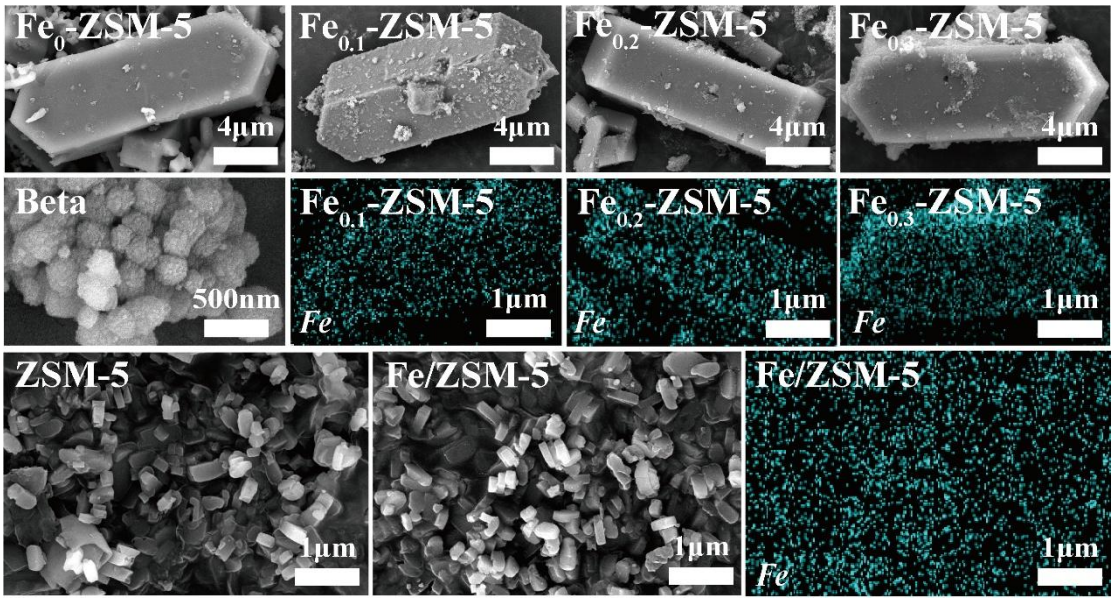


Figure 4 SEM images and EDS mapping of Fe-ZSM-5 synthesized via interzeolite conversion and Fe/ZSM-5 prepared by impregnation, together with Beta and ZSM-5 raw materials

The morphology and crystal size of the catalyst samples were examined by scanning electron microscopy (Figure 4). The original Beta zeolite had a particle size of around 200 nm and a spherical aggregate shape with a rough surface and no clear crystal facets. The Fe_x-ZSM-5 (x = 0, 0.1, 0.2, 0.3) samples all showed the characteristic coffin-shaped morphology of ZSM-5 zeolites, with comparable crystal dimensions of approximately 16 μm × 5 μm × 2 μm. This indicates that the addition of iron had no appreciable impact on the size or morphology of the ZSM-5 zeolite. A few particles were also seen on the crystal surfaces; these could be pieces of the initial Beta material that had not fully transformed into the ZSM-5 structure. The commercial ZSM-5 zeolite exhibits an aggregated, irregular near-elliptical plate-like morphology, with a crystal

size of approximately 500 nm. No significant change in the overall morphology was observed after the impregnation treatment. Elemental analysis of the iron-containing catalyst samples was conducted via EDS spectroscopy. The EDS mapping of Fe (Figure 4) shows that the introduced iron species exhibits uniform dispersion without significant agglomeration. The compositional data summarized in Table 2 indicate that the iron content of the catalyst samples increases progressively with the amount of $FeCl_2$ added during synthesis, despite the subsequent calcination step, whereas the SiO_2/Al_2O_3 ratio remains largely constant at approximately 80. In particular, the Fe loading of the $Fe_{0.3}$-ZSM-5 sample reached as high as 6.48%, and such a high Fe content is crucial for enhancing its catalytic activity in the target reaction.

Table 2 Elemental composition of Fe-ZSM-5 samples with different iron contents synthesized via interzeolite conversion route

Sample	Si (wt%)	Al (wt%)	Fe (wt%)	SiO_2/Al_2O_3 (mol/mol)
$Fe_{0.1}$-ZSM-5	47.0	1.12	3.03	84
$Fe_{0.2}$-ZSM-5	42.5	1.08	4.49	78
$Fe_{0.3}$-ZSM-5	38.3	0.86	6.48	88

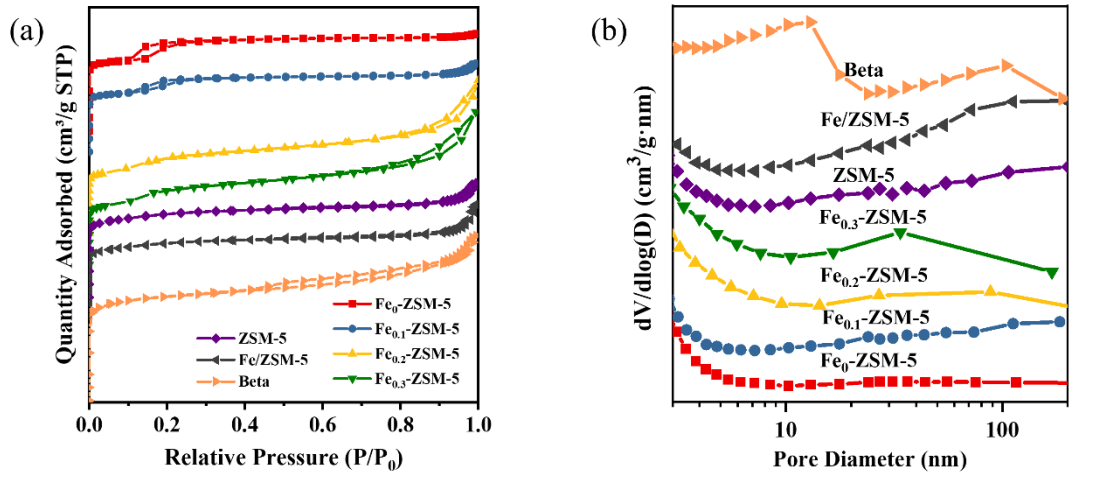


Figure 5 (a) N_2 adsorption-desorption isotherms and (b) pore size distribution curves of Fe_x-ZSM-5 (interzeolite conversion), Fe/ZSM-5 (impregnation), and Beta and ZSM-5 reference samples

As shown in Figure 5(a), all Fe_x-ZSM-5 samples exhibit characteristic type I isotherms, confirming the existence of micropores. With increasing Fe content, the total BET surface area progressively declines from 391 m^2/g (Fe_0-ZSM-5) to 295 m^2/g ($Fe_{0.3}$-ZSM-5), while the micropore surface area drops from 386 to 205 m^2/g (Table 3). This

decrease is attributed to the partial blockage of zeolite micropores by iron oxide species. Simultaneously, the external surface area increases sharply from 5 to 90 m^2/g and the mesopore volume rises from 0.012 to 0.172 cm^3/g, reflecting the formation of intercrystalline mesoporosity arising from unconverted Beta zeolite fragments adhered to the external crystal surface and/or the generation of Fe_xO_y nanoparticles. The pore size distribution (Figure 5(b)) corroborates this evolution: $Fe_{0.1}$-ZSM-5 retains a predominantly microporous character, whereas $Fe_{0.2}$-ZSM-5 and $Fe_{0.3}$-ZSM-5 develop a broad mesopore contribution, consistent with the creation of intercrystalline voids.

Table 3 Specific surface area and pore structure data of Fe/ZSM-5 prepared by impregnation and the series of Fe-ZSM-5 synthesized via interzeolite conversion route

Sample	SSA (m^2/g)			Pore volume (cm^3/g)		
	S_{total}[a]	S_{micro}	S_{ext}[b]	V_{total}[c]	V_{micro}[b]	V_{meso}[d]
Beta	584	520	63	0.337	0.204	0.133
Fe_0-ZSM-5	391	386	5	0.194	0.182	0.012
$Fe_{0.1}$-ZSM-5	335	329	6	0.179	0.152	0.027
$Fe_{0.2}$-ZSM-5	302	221	81	0.261	0.111	0.150
$Fe_{0.3}$-ZSM-5	295	205	90	0.278	0.106	0.172
ZSM-5	421	406	15	0.225	0.170	0.055
Fe/ZSM-5	378	365	13	0.221	0.151	0.070

[a] Total surface area calculated by the BET method.

[b] Calculated by the t-plot method.

[c] Total pore volume calculated from the adsorption amount at $P/P^0 = 0.99$.

[d] $V_{meso} = V_{total} - V_{micro}$

The Fe/ZSM-5 sample prepared by impregnation displays a BET surface area of 378 m^2/g and a micropore surface area of 365 m^2/g, with a modest external surface area of only 13 m^2/g. These values are notably higher than those of $Fe_{0.2}$-ZSM-5 and $Fe_{0.3}$-ZSM-5, indicating that impregnation results in less intrusive textural alteration: the microporous structure is better preserved, with 96.6% of the total surface area contributed by micropores versus 73.2% and 69.5% for $Fe_{0.2}$-ZSM-5 and $Fe_{0.3}$-ZSM-5, respectively. This difference suggests that the interzeolite conversion route promotes more extensive interaction between iron species and the zeolite framework, favoring

iron incorporation both within micropores and on the external surface. In contrast, impregnation predominantly deposits iron species on the external surface with limited micropore penetration, resulting in minimal disruption to the microporous network [34].

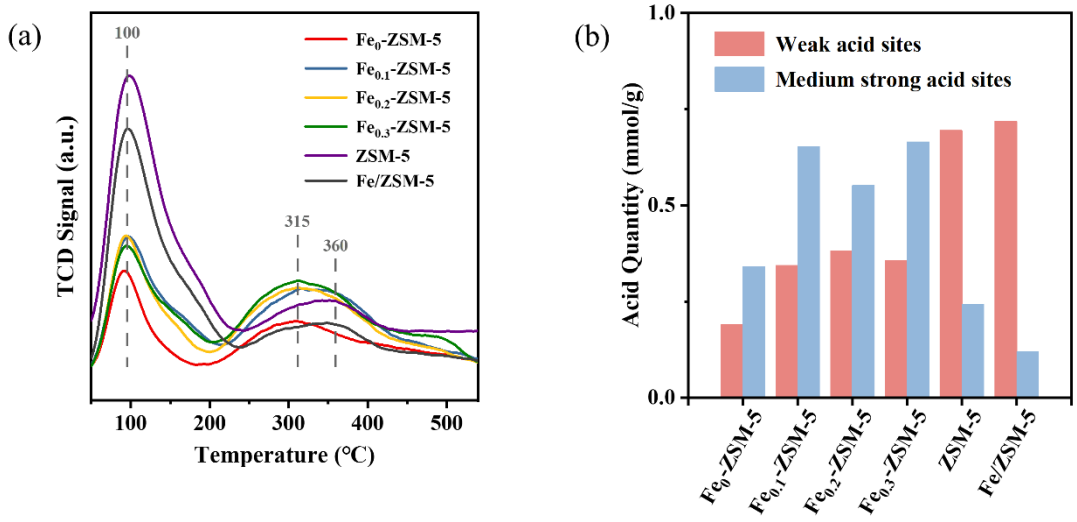


Figure 6 (a) NH_3-TPD profiles and (b) acid site distribution of Fe/ZSM-5 prepared by impregnation and Fe-ZSM-5 synthesized via interzeolite conversion route

The surface acidity of the catalyst samples was determined using NH_3 temperature-programmed desorption (NH_3-TPD), and the results are shown in Figure 6. All zeolite samples exhibited a low-temperature desorption peak and a high-temperature desorption peak. The low-temperature desorption peak centered at approximately 100 °C corresponds to weakly bound NH_3 on weak acid sites, whereas the high-temperature desorption peak in the range of 250-400 °C originates from NH_3 strongly interacting with strong acid sites, which in MFI-type zeolites are predominantly Brønsted acid sites associated with bridging Si-(OH)-Al groups [35].

According to the acid site distribution (Figure 6(b)), medium-strong Brønsted acids predominate in the zeolite samples synthesized via interzeolite conversion route, whereas weak Lewis acids predominate in the commercial ZSM-5 zeolite and Fe/ZSM-5 prepared by impregnation. The peak intensities of all the Fe_x-ZSM-5 (x = 0.1, 0.2, 0.3) were higher than those of the Fe_0-ZSM-5 sample, indicating that the weak and medium-strong acid concentrations of iron-containing samples are higher than those of the iron-free sample. Nonetheless, the NH_3-TPD curves for Fe_x-ZSM-5 (x = 0.1, 0.2, 0.3) samples with varying iron levels had comparable peak intensities and similar shapes, indicating that the acidity within the range examined in this work was not

greatly impacted by the amount of iron loading. On the other hand, Fe/ZSM-5 had fewer acid sites than commercial ZSM-5. It is speculated that the iron species introduced by impregnation have poorer dispersion, and some iron species may cover the acid sites on the zeolite, reducing the accessibility of these sites [36, 37]. A comparison of the acidity profiles of the two samples with comparable iron contents but different incorporation methods reveals that Fe/ZSM-5 contains more weak acid sites but fewer medium-strong acid sites than $Fe_{0.1}$-ZSM-5. Such differences in acid site properties may further influence the catalytic performance of the samples in the target reaction.

In conclusion, both iron incorporation techniques did not change the ZSM-5 framework structure or morphology, according to the characterization results from XRD, FT-IR, Raman, SEM, N_2 physisorption, and NH_3-TPD. However, they did result in decreased crystallinity, reduced micropore surface area, and increased mesopore volume, indicating that iron species may block or damage micropores. For samples synthesized via the interzeolite conversion route, iron incorporation enhanced the acidity, but increasing the iron loading did not significantly impact the acidity further; the impregnation method resulted in lower acidity due to iron covering acid sites.

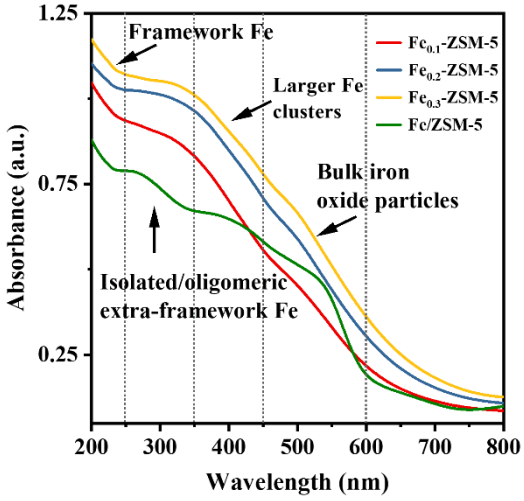


Figure 7 UV-Vis diffuse reflectance spectra of Fe/ZSM-5 prepared by impregnation and Fe-ZSM-5 samples synthesized via interzeolite conversion route

Iron oxide nanoparticles (Fe_2O_3, Fe_3O_4, etc.), oligomeric iron oxide clusters (Fe_xO_y), and isolated iron species (mononuclear or binuclear oxo-bridged iron species) are the most common forms of iron species found in iron zeolites. These particles are commonly found on the outside or inside the zeolite channels [38]. Iron species usually

show strong absorption in the 200-800 nm range in UV-Vis diffuse reflectance spectra: framework iron usually shows absorption bands at 200-250 nm, isolated/oligomeric extra-framework iron species within zeolite channels typically absorb at 250-350 nm, larger iron clusters absorb in the 350-450 nm region, and bulky iron oxide nanoparticles absorb at wavelengths greater than 450 nm [39-41].As shown in Figure 7, all samples exhibit prominent UV-Vis absorbance in the 200-600 nm range, suggesting that isolated framework iron, isolated/oligomeric extra-framework iron and iron oxide clusters of various sizes were present in all four iron-containing samples. Notably, for the Fe_x-ZSM-5 series, the UV-Vis absorption intensity progressively increases with iron content, while the spectral profiles remain nearly unchanged, indicating that the distribution of iron species is largely similar across these samples. In particular, compared to $Fe_{0.1}$-ZSM-5, the Fe/ZSM-5 sample exhibits stronger UV-Vis absorption in the 400-600 nm region but weaker absorption in the 200-400 nm region, suggesting that the former primarily contains isolated framework iron and isolated/oligomeric extra-framework iron, whereas the latter is dominated by larger iron oxide clusters or particles.

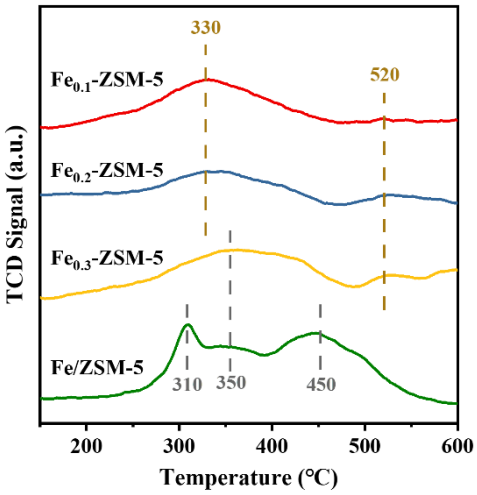


Figure 8 H_2-TPR profiles of Fe/ZSM-5 prepared by impregnation and Fe-ZSM-5 samples synthesized via interzeolite conversion route

As revealed by the H_2-TPR profiles presented in Figure 8, all Fe_x-ZSM-5 (x = 0.1, 0.2, 0.3) samples synthesized via the interzeolite conversion route exhibit two well-defined reduction peaks over the temperature range of 100-600 ℃. Specifically, a broad low-temperature reduction feature centered at approximately 330 ℃ is observed, the maximum of which progressively shifts to higher temperatures with increasing iron

loading, while the high-temperature reduction peak located at around 520 ℃ appears to be relatively minor in intensity. According to the literature, during the calcination of as-synthesized iron-containing zeolites, a portion of the framework iron migrates to extra-framework positions, forming aggregated iron-oxo clusters and even larger-sized bulk iron oxides [42, 43]. Combined with the aforementioned UV-Vis diffuse reflectance spectroscopy results, the low-temperature reduction peak near 330 ℃ can be primarily attributed to the reduction of highly dispersed extra-framework iron species (including isolated and oligomeric iron clusters), whereas the high-temperature reduction peak near 520 ℃ corresponds to the reduction of larger-sized, well-crystallized bulk iron oxides (e.g., Fe_2O_3 particles). Notably, no reduction signals attributable to framework iron are detected in any of the samples, consistent with the generally recognized resistance of tetrahedrally coordinated framework iron toward reduction [44]. In contrast, the H_2-TPR profile of the Fe/ZSM-5 catalyst prepared by incipient wetness impregnation, with an iron content comparable to that of $Fe_{0.1}$-ZSM-5, displays four distinct reduction peaks accompanied by a notably larger H_2 consumption in the high-temperature region. This observation indicates that the iron species in the impregnated sample are poorly dispersed, leading to the formation of a higher proportion of large-sized aggregated iron oxide phases.

The Raman, UV-Vis diffuse reflectance spectra, and H_2-TPR analytical data show that the iron species in the four iron-containing materials are present in a variety of forms. In particular, the iron species in the samples created by incipient wetness impregnation are primarily bigger iron oxide clusters or particles, while the iron species in the samples synthesized by the interzeolite conversion approach are primarily well-dispersed isolated framework iron and extra-framework iron.

Performance of phenol hydroxylation

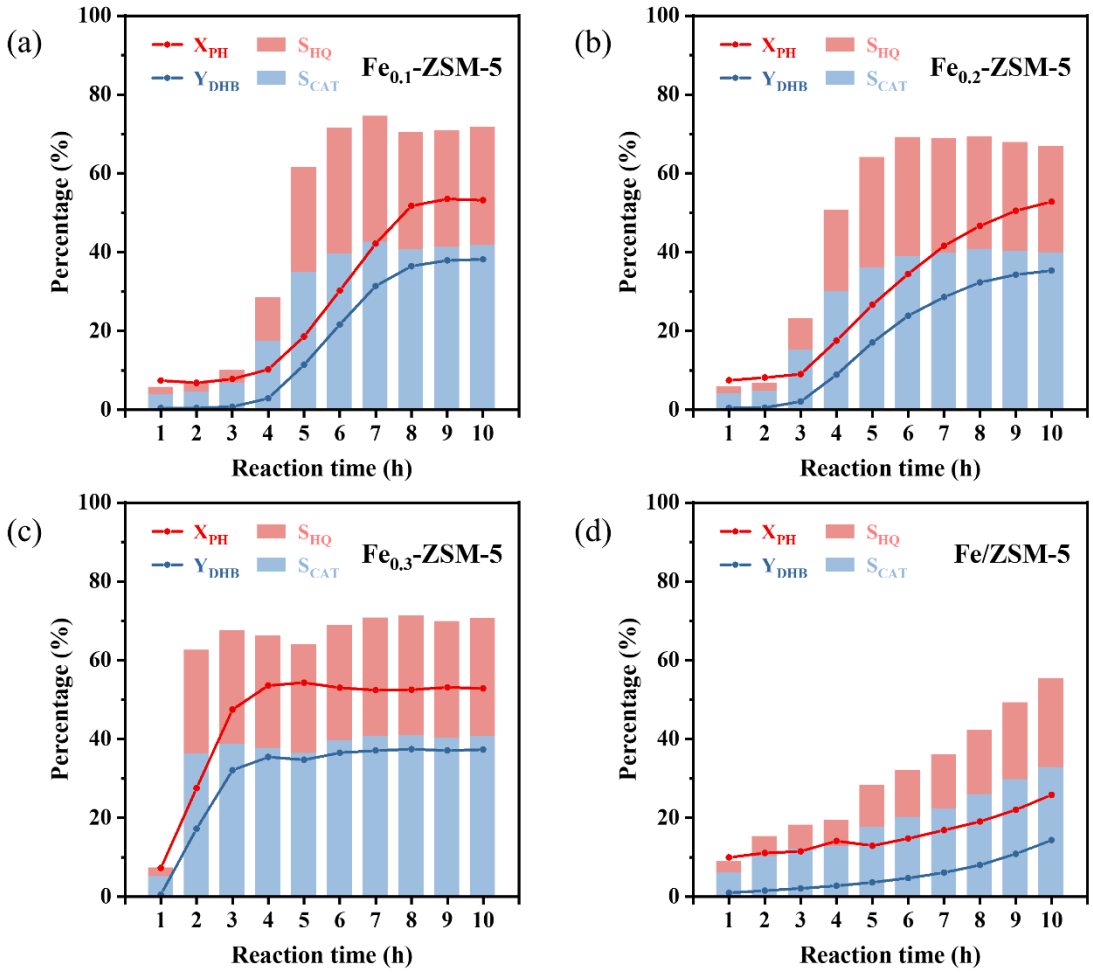


Figure 9 Phenol hydroxylation performance of Fe-ZSM-5 synthesized via interzeolite conversion route and Fe/ZSM-5 by impregnation method. (a) $Fe_{0.1}$-ZSM-5 (b) $Fe_{0.2}$-ZSM-5 (c) $Fe_{0.3}$-ZSM-5 (d) Fe/ZSM-5. Reaction conditions: 2 g phenol, 24 mL H_2O, 0.1 g catalyst in three-necked flask, heated to 50 °C, then 2.25 mL H_2O_2 (aq) added

The catalytic performance of the iron-containing catalyst samples in the phenol hydroxylation reaction was evaluated over a period of 10 h. As shown in Figure 9(a)-(c), all Fe_x-ZSM-5 catalysts exhibit a pronounced induction period of approximately 1-3 h, during which both the phenol conversion and dihydroxybenzene (DHB, i.e., catechol and hydroquinone) selectivity remain at low levels. This induction period can be attributed to the synergistic effect of two factors: (i) Micropore diffusion limitations. The pore size of ZSM-5 (~0.55 nm) is comparable to the kinetic diameter of phenol (~0.58 nm) [10, 45], necessitating a finite time for phenol to diffuse into the zeolite channels and establish adsorption-desorption equilibrium at the active sites. (ii) In situ activation of iron species. In the freshly calcined Fe_x-ZSM-5 catalysts, iron predominantly exists as Fe^{3+}, whereas the efficient generation of hydroxyl radicals

(·OH) requires Fe^{2+}. During the initial stage of the reaction, Fe^{3+} must be progressively reduced to Fe^{2+} by the reaction medium (phenol, water, or H_2O_2 itself). Once the steady-state concentration of Fe^{2+} is attained and adsorption-desorption equilibrium is established, the reaction rate increases markedly, giving rise to the characteristic S-shaped kinetic curve [6]. Notably, the induction period of $Fe_{0.3}$-ZSM-5 is significantly shorter than those of the other two samples, which can be ascribed to the higher content of oligomeric iron clusters in the sample with greater iron loading. Compared to isolated framework Fe^{3+} sites, such iron clusters are more readily reducible and therefore capable of activating H_2O_2 more rapidly [46].

After the induction period, as the reaction proceeds, the phenol conversion, DHB yield, and the selectivities to catechol and hydroquinone over Fe_x-ZSM-5 (x = 0.1, 0.2, 0.3) all exhibit a gradual upward trend. At a reaction time of 10 h, these catalytic performance metrics for each catalyst approach a plateau and are comparable to one another. This result can be attributed to the similar crystallinity, textural parameters, and acidic and redox properties of the three catalysts. Among them, $Fe_{0.1}$-ZSM-5 achieves the highest phenol conversion of 53.51%, the maximum target product yield of 38.18%, and the highest total DHB selectivity of 74.52% (S_{CAT} = 42.59%, S_{HQ} = 31.93%), with dark-colored tar as the primary byproduct. However, the catalytic performance of this catalyst, particularly the DHB selectivity, is notably lower than our previously reported results (S_{DHB} = 95.6%) [47]. The origins of this discrepancy will be analyzed in depth in a later section.

For comparison, Fe/ZSM-5 with an iron loading comparable to that of $Fe_{0.1}$-ZSM-5 was prepared by the impregnation method, and its catalytic performance is shown in Figure 9(d). In contrast to $Fe_{0.1}$-ZSM-5 synthesized via the interzeolite transformation route, Fe/ZSM-5 exhibits a maximum phenol conversion of only 25.83%, a maximum product yield of 14.33%, and a total DHB selectivity of merely 55.46% (S_{CAT} = 32.85%, S_{HQ} = 22.62%). The aforementioned characterization results indicate that the two catalysts exhibit only minor differences in crystallinity and textural parameters, with the primary distinctions lying in the type of iron species and acidity. Extensive literature on iron-based catalysts for phenol hydroxylation has demonstrated that acidity plays a

crucial promotional role in this reaction. A study on Fe/Al-AMS catalysts reported that Lewis acid sites generated by framework Al facilitate the enhanced generation of ·OH during the reaction, thereby improving catalytic performance [48]. Another study indicated that the presence of protonic acid sites in Fe-ZSM-5 favors the formation of p-benzoquinone, whereas the substitution of acidic protons by Fe cations possessing Lewis acidity—and the consequent reduction in acid site concentration—leads to enhanced selectivity toward catechol and hydroquinone [49]. Based on these results, it can be inferred that the lower phenol conversion of Fe/ZSM-5 prepared by impregnation is associated with its poorer dispersion of iron species, whereas the product selectivity is primarily governed by acidity. Compared to $Fe_{0.1}$-ZSM-5, Fe/ZSM-5 possesses fewer strong protonic acid sites and a significantly higher concentration of weak Lewis acid centers, yet exhibits markedly lower DHB selectivity. The above results suggest that the conclusions reported in the literature concerning the influence of catalyst acidity on DHB selectivity remain controversial.

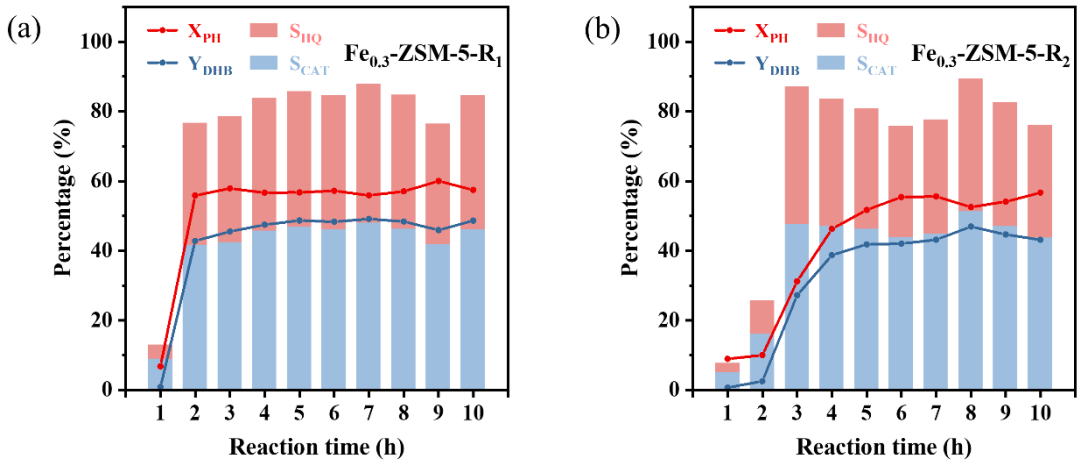


Figure 10 Hydroxylation performance of phenol over the $Fe_{0.3}$-ZSM-5 catalyst sample after (a) one regeneration cycle and (b) two regeneration cycles

Given that $Fe_{0.3}$-ZSM-5 exhibits the fastest catalytic reaction rate, this catalyst was selected for further stability evaluation. After 10 h of reaction, $Fe_{0.3}$-ZSM-5, isolated by centrifugation, turned from its original brownish-yellow color to black due to coverage by tar on its surface. The spent catalyst was regenerated by calcination in a muffle furnace at 550 ℃ in air for 1 h, during which its color reverted from black to a light yellow. The regenerated catalyst exhibits a lighter color, suggesting that iron species

not incorporated into the zeolite framework in the fresh $Fe_{0.3}$-ZSM-5 catalyst were substantially leached during the phenol hydroxylation reaction. The catalytic performance of the regenerated catalyst in phenol hydroxylation was then evaluated under identical reaction conditions, and the results are shown in Figure 10. Both regenerated samples exhibit superior catalytic performance compared to the fresh catalyst. The once-regenerated sample, $Fe_{0.3}$-ZSM-5-R_1, achieves a maximum phenol conversion of 54.57%, a maximum DHB yield of 44.67%, and a highest total selectivity of 87.89% (S_{CAT} = 47.90%, S_{HQ} = 39.92%). The twice-regenerated sample exhibits comparable performance, with a maximum phenol conversion of 51.52%, a maximum DHB yield of 42.68%, and a highest total selectivity of 89.35% (S_{CAT} = 51.26%, S_{HQ} = 38.09%).

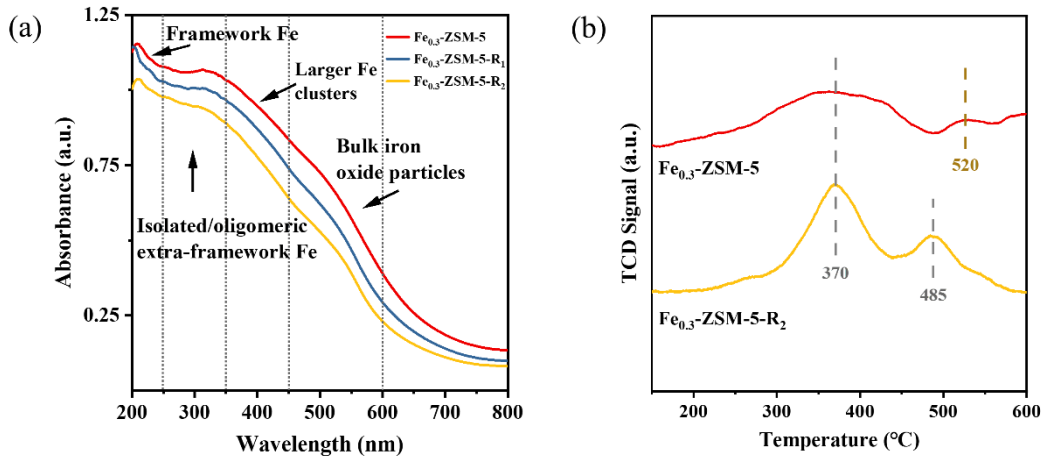


Figure 11 UV-Vis spectra of the $Fe_{0.3}$-ZSM-5 catalyst after (a) one regeneration cycle and two regeneration cycles, and (b) H_2-TPR profile of the sample after two regeneration cycles

To elucidate the origin of the enhanced DHB selectivity of the regenerated catalysts, UV-Vis diffuse reflectance spectroscopy (UV-Vis DRS) was first employed to characterize the regenerated samples, and the results are shown in Figure 11(a). The spectral profiles of $Fe_{0.3}$-ZSM-5 before and after regeneration are similar, although the band intensity decreases slightly with increasing regeneration cycles, indicating that the types of iron species in the sample do not undergo significant changes, with only a modest reduction in iron content. Subsequently, H_2-TPR was performed to evaluate the reducibility of the regenerated samples, and the results are shown in Figure 11(b). Compared with fresh $Fe_{0.3}$-ZSM-5, the reduction profiles of the regenerated samples

exhibit pronounced changes: the low-temperature reduction peak at 370 ℃ becomes markedly narrower and more intense, suggesting that iron species weakly bound to the zeolite framework may undergo partial leaching into the solution during the reaction. It is well established that H^+ is generated in the phenol hydroxylation reaction system catalyzed by iron-containing zeolites, and the pH of the reaction medium gradually shifts from neutral to acidic as the reaction proceeds [50]. pH measurements show that the pH of the fresh $Fe_{0.3}$-ZSM-5 catalytic system drops to approximately 3 after 10 h of reaction. Evidently, such an acidic environment leads to the gradual dissolution of weakly framework-bound iron species into the solution [51]. According to reports, iron ions in solution can catalyze the formation of substantial amounts of tar from phenol, thereby significantly reducing the DHB selectivity [52]. Therefore, the relatively low DHB selectivity of fresh $Fe_{0.3}$-ZSM-5 primarily originates from the leaching of iron species during the reaction. Since the acid-labile iron species are largely removed during the initial reaction cycle, the DHB selectivity over the regenerated catalyst is thus enhanced.

In addition, the acidic property of the regeneration catalyst $Fe_{0.3}$-ZSM-5-R_1 was also measured by NH_3-TPD, and the results are shown in Figure 12. It was found that the density of strong acidic sites is significantly decreased. This suggests that a decrease in the number of Brønsted acid sites may be beneficial for improving dihydroxybenzene selectivity. However, our earlier work showed that the selectivity to dihydroxybenzene increased with increasing Brønsted acid density [47], which is contrary to the trend observed here. This implies that the selectivity is influenced by both the iron speciation and the acidic properties, and that the different iron species present in the two studies may have obscured the true role of acid density. To clarify the independent effect of acidic properties on the dihydroxybenzene selectivity, catalysts containing a single type of active iron species with a tunable acid density are required; such investigations are currently in progress in our laboratory.

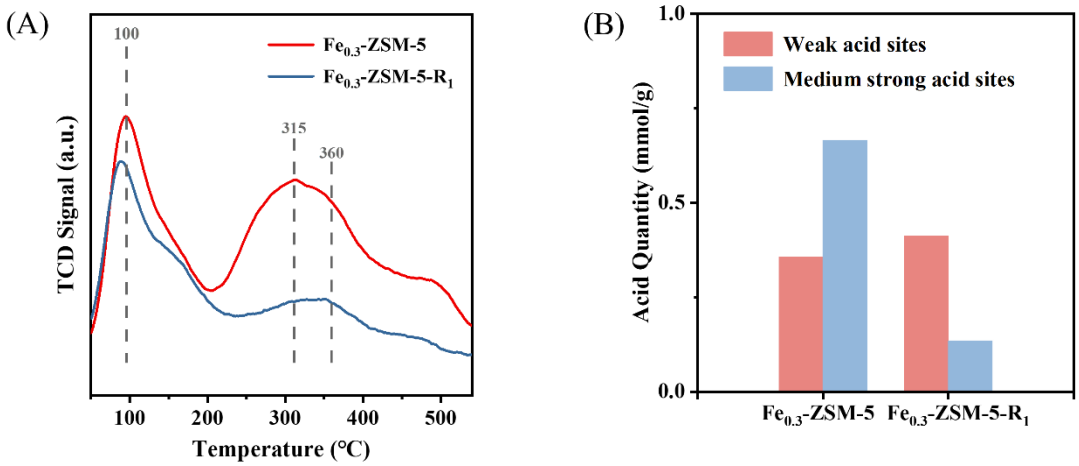


Figure 12 (a) NH_3-TPD profiles and (b) acid site distribution of Fe/ZSM-5 prepared by impregnation and Fe-ZSM-5 synthesized via interzeolite conversion route

CONCLUSION

In this study, Fe_x-ZSM-5 (x = 0-0.3) zeolites were successfully synthesized via interzeolite conversion of Beta zeolite in an ionothermal system (Beta: NH_4F: TPABr: Seed: ILs: H_2O = 0.8:1.0:0.304:0.02:5.0:0.304, 180 ℃, 96 h). Iron in Fe_x-ZSM-5 predominantly exists as highly dispersed isolated framework Fe^{3+} and isolated /oligomeric extra-framework Fe_xO_y clusters. In contrast, Fe/ZSM-5 prepared by impregnation contains larger iron oxide aggregates on the external surface.

In phenol hydroxylation, $Fe_{0.1}$-ZSM-5 achieves a conversion of 53.51% and dihydroxybenzene selectivity of 74.52%, significantly outperforming Fe/ZSM-5 (25.83% and 55.46%). This is attributed to higher iron dispersion in $Fe_{0.1}$-ZSM-5. Regenerated $Fe_{0.3}$-ZSM-5 shows enhanced dihydroxybenzene selectivity up to 89.35%, attributed to the removal of acid-labile iron species (suppressing tar formation).

COMPETING INTERESTS

Authors declare no competing interests.

ACKNOWLEDGEMENTS

This work was supported by the National Natural Science Foundation of China (No. 22168022) and the Basic Research Innovation Group Project of Gansu Province, China (No. 22JR5RA219).

REFERENCES

[1] Krumenacker L, Costantini M, Pontal P et al (1996) Kirk-Othmer Encyclopedia of Chemical Technology. Wiley, New York

[2] Adam F, Wong JT and Ng EP (2013) Fast catalytic oxidation of phenol over iron modified zeolite L nanocrystals. Chemical Engineering Journal 214:63-67. DOI: 10.1016/j.cej.2012.10.017

[3] Villa AL, Caro CA and Correa CM (2004) Cu- and Fe-ZSM-5 as catalysts for phenol hydroxylation. Journal of Molecular Catalysis A: Chemical 228:233-240. DOI: 10.1016/j.molcata.2004.09.035

[4] Romano U and Ricci M (2008) Handbook of Heterogeneous Catalysis. Wiley, Weinheims

[5] Salazar-Aguilar AD, Vega G, Casas JA et al (2020) Direct Hydroxylation of Phenol to Dihydroxybenzenes by H_2O_2 and Fe-based Metal-Organic Framework Catalyst at Room Temperature. Catalysts 10:172-186. DOI: 10.3390/catal10020172

[6] Naranov E, Ramazanov D, Agliullin M et al (2024) Recent Advances in Aromatic Hydroxylation to Phenol and Hydroquinone Using H_2O_2. Catalysts 15:36-58. DOI: 10.3390/molecules27175457

[7] Chavez Rivas F, Rodriguez-Iznaga I, Concepcion-Rosabal B et al (2019) Fe Speciation in Iron Modified Natural Zeolites as Sustainable Environmental Catalysts. Catalysts 10:1-14. DOI: 10.3390/catal9100866

[8] Zhang J, Tang X, Yi H et al (2022) Synthesis, characterization and application of Fe-zeolite: A review. Applied Catalysis A: General 630:118467. DOI: 10.1016/j.apcata.2021.118467

[9] Hu ZP, Chen L, Chen C et al (2018) Fe/ZSM-5 catalysts for ammonia decomposition to CO_x-free hydrogen: Effect of SiO_2/Al_2O_3 ratio. Molecular Catalysis 455:14-22. DOI: 10.1016/j.mcat.2018.05.027

[10] Ayari F, Mhamdi M, Alvarez-Rodriguez J et al (2012) Influence of the parent zeolite structure on chromium speciation and catalytic properties of Cr-zeolite catalysts in the ethylene ammoxidation. Applied Catalysis A: General 439-440:88-100. DOI: 10.1016/j.apcata.2012.06.037

[11] Han ZY, Zhang F and Zhao XH (2019) Green energy-efficient synthesis of Fe-ZSM-5 zeolite and its application for hydroxylation of phenol. Microporous and Mesoporous Materials 290:109679. DOI: 10.1016/j.micromeso.2019.109679

[12] Tang L, Haw KG, Zhang Y et al (2019) Fast and efficient synthesis of SSZ-13 by interzeolite conversion of Zeolite Beta and Zeolite L. Microporous and Mesoporous Materials 280:306-314. DOI: 10.1016/j.micromeso.2019.02.021

[13] Jakupce N, Ardila-Fierro KJ, Martinez V et al (2024) Mechanochemically Induced OSDA-Free Interzeolite Conversion. ACS Sustainable Chemistry & Engineering 12:5220-5228. DOI: 10.1021/acssuschemeng.3c08477

[14] Goel S, Zones SI, Iglesia E (2015) Synthesis of zeolites via interzeolite transformations without organic structure-directing agents. Chemistry of Materials 27:2056-2066. DOI: 10.1021/cm504510f

[15] Catlow CRA, Coombes DS, Lewis DW et al (2003) Handbook of Zeolite Science and Technology. Marcel Dekker, New York
[16] Wang Y, Tong C, Liu Q et al (2023) Intergrowth Zeolites: Synthesis, Characterization, and Catalysis. Chemical Reviews 123:11664-11721. DOI: 10.1021/acs.chemrev.3c00373
[17] Zhang L, Weng X, Qu X et al (2019) Efficient removal of ionic liquids from aqueous media using ZSM-5 zeolites: A tunable mechanism combining micropore filling and electrostatic interaction. Microporous and Mesoporous Materials 280:315-323. DOI: 10.1016/j.micromeso.2019.02.004
[18] Cooper ER, Andrews CD, Wheatley PS et al (2004) Ionic liquids and eutectic mixtures as solvent and template in synthesis of zeolite analogues. Nature 430:1012-1016. DOI: 10.1038/nature02860
[19] Bensafi B, Chouat N, and Djafri F (2023) The universal zeolite ZSM-5: Structure and synthesis strategies. A review. Coordination Chemistry Reviews 496:215397. DOI: 10.1016/j. ccr.2023.215397
[20] Yang Z, Li Y, Wang D et al (2022) Interzeolite conversion of HY to hierarchical HZSM-5 catalyst via an ionothermal route and its excellent catalytic performance in methanol-to-aromatics reaction. Journal of Porous Materials 29:1039-1047. DOI: 10.1007/s10934-022-01227-z
[21] Bachari K, Millet JMM, Benaichouba B et al (2004) Benzylation of benzene by benzyl chloride over iron mesoporous molecular sieves materials. Journal of Catalysis 221:55-61. DOI: 10.1016/s0021-9517(03)00295-1
[22] Zhou L, Li HJ, Wang JQ et al (2021) FeAlPO-34 molecular sieves with controllably high iron contents: ionothermal synthesis and catalytic performance in phenol hydroxylation. Desalination and Water Treatment 220:309-315. DOI:10.5004/dwt.2021.26984
[23] Chukanov NV and Chervonnyi AD (2016) Infrared Spectroscopy of Minerals and Related Compounds. Springer International Publishing, Switzerland
[24] Figueiredo AL, Araujo AS, Linares M et al (2016) Catalytic cracking of LDPE over nanocrystalline HZSM-5 zeolite prepared by seed-assisted synthesis from an organic-template-free system. Journal of Analytical and Applied Pyrolysis 117:132-140. DOI: 10.1016/j.jaap.2015. 12.005
[25] Mukaromah AH, Kadja GTM, Mukti RR et al (2016) Buchari, Surface-to-volume ratio of synthesis reactor vessel governing low temperature crystallization of ZSM-5. Journal of Materials Science 48:241-251. DOI: 10.5614/j.math.fund.sci.2016. 48.3.5
[26] Niu XR, Li J, Zhang Z et al (2017) ZSM-5 functionalized in situ with manganese ions for the catalytic oxidation of cyclohexane. RSC Advances 7:50619-50625. DOI: 10.1039/c7ra10771d
[27] Wakabayashi F, Kondo JN, Domen K et al (1996) An attempt to a semi-quantitative analysis of Lewis acid sites in H-ZSM-5 zeolite using water as an IR-spectroscopic titrant. Catalysis Letters 38:15-19. DOI: 10.1007/bf00806893

[28] Fan F, Sun K, Feng Z et al (2009) From Molecular Fragments to Crystals: A UV Raman Spectroscopic Study on the Mechanism of Fe-ZSM-5 Synthesis. Chemistry-A European Journal 15:3268-3276. DOI: 10.1002/chem.200801916
[29] Dutta PK and Puri M (1987) Synthesis and Structure of Zeolite ZSM-5: A Raman Spectroscopic Study. The Journal of Physical Chemistry 91:4329-4333. DOI: 10.1021/j100300a025
[30] Yu Y, Xiong G, Li C et al (2000) Characterization of Iron Atoms in the Framework of MFI-Type Zeolites by UV Resonance Raman Spectroscopy. Journal of Catalysis 194:487-490. DOI: 10.1006/jcat.2000.2946
[31] Marshall CP, Dufresne WJB and Ruffledt CJ (2020) Polarized Raman spectra of hematite and assignment of external modes. Journal of Raman Spectroscopy 51:1522-1529. DOI: 10.1002/jrs.5824
[32] Fan F, Xu Q, Xia H et al (2009) UV Raman Spectroscopy Study of Catalytic Materials. Chinese Journal of Catalysis 30:717-739. DOI: 10.1360/972009-470
[33] Ali M, Kim JJ, Zafar F et al (2023) Effects of ZSM-5 Morphology and Fe Promoter for Dimethyl Ether Conversion to Gasoline-Range Hydrocarbons. Catalysts 13:910. DOI: 10.3390/catal13050910
[34] Wang XT, Hu HP, Zhang XY et al (2019) Effect of iron loading on the performance and structure of FeZSM-5 catalyst for the selective catalytic reduction of NO with NH3. Environmental Science and Pollution Research 26:1706-1715. DOI:10.1007/s11356-018-3513-x
[35] Bai Y, Wu W and Bian X (2017) Investigation of the interactions in CeO_2-Fe_2O_3 binary metal oxides supported on ZSM-5 for NO removal by CO in the presence of O_2, SO_2 and steam. *RSC Advances* **7**:56447-56456. DOI: 10.1039 /c7ra10773k
[36] Liu YJ, Bolshakov A, Coza M et al (2023) Isomorphously Substituted [Fe,Al]ZSM-5 Catalysts for Methane Dehydroaromatization. ACS Catalysis 13:8128-8138. DOI: 10.1021/ acscatal.3c00854
[37] Hosseinpour M, Akizuki M, Yok A et al (2020) Novel synthesis and characterization of Fe-ZSM-5 nanocrystals in hot compressed water for selective catalytic reduction of NO with NH_3. Microporous and Mesoporous Materials 292:109708. DOI: 10.1016/j.micromeso.2019.109708
[38] Reyes Villegas VA, De León Ramirez JI, Pérez-Cabrera L et al (2025) Sonochemical post-synthesis modification of Y zeolite with iron species. Materials Chemistry and Physics 331:130199. DOI: 10.1016/j.matchemphys.2024.130199
[39] Cheng Q, Li G, Yao X et al (2023) Maximizing Active Fe Species in ZSM-5 Zeolite Using Organic-Template-Free Synthesis for Efficient Selective Methane Oxidation. Journal of the American Chemical Society 145:5888-5898. DOI: 10.1021/jacs. 2c13351
[40] Berlier G, Crocellà V, Signorile M et al (2018) Structure and Reactivity of Metals in Zeolite Materials. Springer International Publishing, Cham
[41] Liu J, Cheng H, Zheng H et al (2021) Insight into the Potassium Poisoning Effect for Selective Catalytic Reduction of NO_x with NH_3 over Fe/Beta. ACS Catalysis 11:14727-14739. DOI:10.1021/acscatal.1c04497

[42] Battiston AA, Bitter JH, de Groot FMF et al (2003) Evolution of Fe species during the synthesis of over-exchanged Fe/ZSM5 obtained by chemical vapor deposition of $FeCl_3$. Journal of Catalysis 213:251-271. DOI:10.1016/s0021-9517(02)00051-9

[43] Pérez-Ramírez J, Mul G, Kapteijn F et al (2002) Physicochemical Characterization of Isomorphously Substituted FeZSM-5 during Activation. Journal of Catalysis 207:113-126. DOI: 10.1006/jcat.2002.3511

[44] Pérez-Ramírez J, Groen JC, Brückner A et al (2005) Evolution of isomorphously substituted iron zeolites during activation: comparison of Fe-beta and Fe-ZSM-5. Journal of Catalysis 232:318-334. DOI: 10.1016/j.jcat.2005.03.018

[45] Shakeri M and Bakhodaye Dehghanpour S (2020) Rational synthesis of TS-1 zeolite to direct both particle size and framework Ti in favor of enhanced catalytic performance. Microporous and Mesoporous Materials 298:110066. DOI: 10.1016/j.micromeso.2020.110066

[46] Fajerwerg K, Foussard JN, Perrard A et al (1997) Wet oxidation of phenol by hydrogen peroxide: the key role of pH on the catalytic behaviour of Fe-ZSM-5. Water Science and Technology 35:103-110. DOI: 10.2166/ wst.1997.0096

[47] Ding MQ, Zhao XH, Li YR et al (2026) Synergistic octahedral iron and Brønsted acid sites in Fe-ZSM-5 for selective phenol hydroxylation to dihydroxybenzenes. ACS Catalysis 16:7592-7610. DOI: 10.1021/acscatal.6c00216

[48] Zhou SJ, Shao B, Jin WM et al (2019) Acid-redox bifunctional Fe/Al-AMS catalyst: Simultaneously oriented introducing Fe_2O_3 in the channels and Al in the framework of AMS and its enhanced catalytic performance. Applied Catalysis A: General 575:159-169. DOI: 10.1016/j.apcata.2019.02.022

[49] Li JPH, Kennedy E and Stockenhuber M (2014) Oxidative Coupling and Hydroxylation of Phenol over Transition Metal and Acidic Zeolites: Insights into Catalyst Function. Catalysis Letters 144:9-15. DOI: 10.1007/s10562-013-1142-z

[50] Jiang SS, Zhang HP, Yan Y et al (2015) Stability and deactivation of Fe-ZSM-5 zeolite catalyst for catalytic wet peroxide oxidation of phenol in a membrane reactor. RSC Advances 5:41269-41277. DOI: 10.1039/c5ra05039a

[51] Deng YF and Veser G (2023) Toward Accelerated Activation of Fe-ZSM-5 in Methane Dehydroaromatization. Energy & Fuels 37:13282-13295. DOI: 10.1021/ acs.energyfuels.3c01790

[52] Chellal K, Bachari K and Sadi F (2014) Iron Incorporated Mesoporous Molecular Sieves Synthesized by a Microwave-Hydrothermal Process and Their Application in Catalytic Oxidation. Journal of Cluster Science 143:523-539. DOI: 10.1007/ s10876-013-0632-x